Large Bulk Photovoltaic Response by Symmetry-Breaking Structural Transformation in Ferroelectric $[Ba(Zr_{0.2}Ti_{0.8})O_3]_{0.5}[(Ba_{0.7}Ca_{0.3})TiO_3]_{0.5}$

Atal Bihari Swain, D. Murali, B.R.K. Nanda, and Pattukkannu Murugavel[*]
Department of Physics, Indian Institute of Technology Madras, Chennai 600036, India

(Received 14 June 2018; revised manuscript received 18 November 2018; published 3 April 2019)

The photovoltaic effect in noncentrosymmetric ferroelectrics is gaining much research interest due to its remarkable above band-gap photovoltage. Among the available ferroelectric systems, the $0.5Ba(Zr_{0.2}Ti_{0.8})O_3$-$0.5(Ba_{0.7}Ca_{0.3})TiO_3$ with its high piezocoefficient is considered as an attractive lead-free multifunctional ferroelectric material. The photovoltaic studies on this compound reveal the discovery of a large photogenerated electric field of $368\ \mathrm{V\,cm^{-1}}$, one of the highest values reported in polycrystalline ferroelectric systems. It is demonstrated that the large photovoltaic response in this ferroelectric system is due to the symmetry breaking structural transformation from the tetragonal to rhombohedral and orthorhombic phases. Density functional calculations show that this symmetry breaking transformation leads to the reduction of electron and hole effective masses and delocalization and reorientation of the conduction charge cloud along the polarization direction, which, in turn, gives a high photovoltaic response.

DOI: 10.1103/PhysRevApplied.11.044007

I. INTRODUCTION

The increasing energy demand with limited available fossil energy resources necessitates researchers to venture into viable alternative energy sources. In this context, solar cells, which provide a clean, abundant, and renewable energy source, are the priority area of research in modern science. The choice of materials and mechanism for the electron-hole pair generation upon light illumination followed by their separation and collection before recombination has resulted in the evolution of solar cells from conventional semiconductor p-n junctions to numerous other types, such as organic dye sensitized, polymer, organic, and inorganic perovskite solar cells [1]. However, the recombination of photo-excited carriers severely affects the open-circuit voltage (V_{OC}) and any attempts to minimize it require a high grade of engineering, which eventually makes the device more complex. In addition, the restriction on the V_{OC} imposed by the band gap of the active material limits the efficient functioning of these devices. The innovative photovoltaic (PV) phenomenon observed in ferroelectric materials with a large photo-generated electric field is free from these drawbacks and is believed to be the basis for next-generation photovoltaic devices. However, the ferroelectric systems exhibiting a large PV response are few in number as they are limited to $LiNbO_3$ (LNO) [2], $BaTiO_3$ (BTO) [3], $BiFeO_3$ (BFO) [4], $Pb(Zr_{1-x}Ti_x)O_3$ (PZT) [5], $(Pb_{0.97}La_{0.03})(Zr_{0.52}Ti_{0.48})O_3$ (PLZT) [6], $KBiFe_2O_5$ (KBFO) [7], and $Ba_{1-x}(Bi_{0.5}Li_{0.5})_xTiO_3$ (BBLT) [8]. Several mechanisms have been proposed for the observed large PV response in ferroelectric systems [9,10]. Earlier reports claim that the above band-gap large bulk photovoltaic effect (BPVE) observed in various ferroelectric systems is attributed to the poling-induced internal electric field [11,12]. However, the prominent ones that explain the BPVE are the ballistic and the shift current models [3,13–16]. For example, the highest PV response (open-circuit electric field, $E_{OC} \sim 10^5\ \mathrm{V\,cm^{-1}}$) in a single crystalline Fe-doped LNO sample reported by Glass *et al.* is explained by the ballistic mechanism [17]. The ballistic mechanism is associated with nonthermalized excitation of photoelectrons in a noncentrosymmetric system, which provides an asymmetric momentum distribution of these carriers in the conduction band [17]. Interestingly, Spanier *et al.* demonstrated the bulk BPVE in a BTO single crystalline sample with a power conversion efficiency exceeding the Shockley–Queisser limit [3]. They attributed this effect to the manifestation of the shift current mechanism of the BPVE. According to the shift current mechanism, the generated charge carriers make an interband transition in a noncentrosymmetric system with a virtual shift of the momentum vector in real space and thereby yield a large PV response [3,13–16].

Interestingly, the correlation between the electronic structure of noncentrosymmetric materials and the photocurrent response in terms of shift current has been established by Wang *et al.* for different phases in $KNbO_3$ (KNO) and $(K, Ba)(Ni, Nb)O_{3-\delta}$ (KBNNO) systems [18]. Their calculations suggest that ferroelectric systems having

---

[*] muruga@iitm.ac.in

rhombohedral (*R*) and orthorhombic (*O*) symmetry show a higher shift current coefficient than systems with tetragonal (*T*) symmetry. This indicates that the *R* and *O* phases are more favorable to yield a large photoresponse than the *T* phase in ferroelectric materials. The large photovoltaic response reported in lanthanum-modified PZT morphotropic phase boundary composition, where the *R* and *T* phases coexist, further motivates the search for a piezoelectric system with morphotropic phase boundary (MPB) composition to understand the PV response with respect to the structural symmetries [19].

In this context, the lead-free ferroelectric system, $0.5\mathrm{Ba(Zr_{0.2}Ti_{0.8})O_3}$-$0.5\mathrm{(Ba_{0.7}Ca_{0.3})TiO_3}$ (BZT-BCT) [20], exhibiting a large piezocoefficient ($d_{33} \sim 620$ pC $\mathrm{N^{-1}}$), attracts tremendous research interest due to its intriguing physical properties such as large energy storage density [21], better electrocaloric effect [22], highest electro-optic [23] properties, and so on. Additionally, the existence of MPB in this compound (where *T*, *O*, and *R* phases coexist), creates a favorable condition for the shift current mechanism, which may lead to a large photoresponse. Interestingly, the reported tuneable structural phase transformation by an electric field at MPB [24–26], which produces large structural frustration among coexisting phases, enables us to propose this material as a model system to investigate the photovoltaic effect and its structural correlation. In this work, we discover a large BPVE on a BZT-BCT polycrystalline bulk sample with 18.4 V ($E_{\mathrm{OC}} = 368\ \mathrm{V\,cm^{-1}}$) as the open-circuit voltage (V_{OC}), which is around six times larger compared to that of the parent polycrystalline BTO [27]. Notably, PV studies carried out as a function of poling fields reveal a strong correlation between the PV response and the crystal symmetry in the BZT-BCT ferroelectric system. The density functional theory (DFT) calculations validate the relation between the PV response and the crystal symmetry.

II. METHODS

A. Experimental methods

The $0.5\mathrm{Ba(Zr_{0.2}Ti_{0.8})O_3}$-$0.5\mathrm{(Ba_{0.7}Ca_{0.3})TiO_3}$ sample is fabricated using a conventional solid-state method. A stoichiometric mixture of initial precursors $\mathrm{BaCO_3}$ (purity ≥ 99.9%), $\mathrm{TiO_2}$ (purity ≥ 99.9%), $\mathrm{BaZrO_3}$ (purity ≥ 99.9%), and $\mathrm{CaCO_3}$ (purity ≥ 99.9%) is calcined at 1350 °C for 4 h. Then the calcined powder is ground for better homogeneity, uniaxially pressed into 12-mm-diameter pellets, and sintered at 1450 °C for 4 h.

The powdered samples are subjected to powder x-ray diffraction (XRD) experiments for phase confirmation by employing a Rigaku SmartLab x-ray diffractometer. The XRD patterns are refined using FULLPROF software. The temperature-dependent dielectric permittivity is obtained from the Novocontrol impedance analyzer in the 10 Hz to 10 MHz frequency range. The polarization (*P*) measurements with respect to the electric field (*E*) are carried out by a Radiant Technology *P*-*E* loop tracer. For optical band-gap measurements, a diffused reflectance spectroscopy experiment is performed using the Ultraviolet-Visible-Near Infrared (Jasco) Spectro-Photometer. The samples are polished and cut into dimensions of $7 \times 7 \times 0.5\ \mathrm{mm^3}$ for photovoltaic measurements. On the top side of the sample, a Ag electrode in finger geometry (finger size of 100-μm width separated by a 200-μm gap) is deposited by thermal evaporation technique using a shadow mask and the bottom side is coated with Ag paint. PV measurements are carried out by employing a xenon-arc lamp (Newport, Model No. 67005) as the light source and a Keithley electrometer (6517B) as the measuring unit.

B. Computational details

The presented DFT calculations are performed using the pseudopotential (PP)-based Vienna *ab-initio* simulation package (VASP) [28]. PPs are based on the projected augmented wave (PAW) [29] method with exchange and correlation effects described using a generalized gradient approximation (GGA) and Perdew-Burke-Ernzerhof (PBE) functional [30,31]. For the elements present in our model, the following valance electrons are explicitly considered in the PP: Ba-$4s^2\ 4p^6\ 5s^2$, Ca-$3p^6\ 4s^2$, Zr-$4p^6\ 4d^2\ 5s^2$, Ti-$3p^6\ 3d^2\ 4s^2$, and O-$2s^2\ 2p^4$. The plane wave cut-off energy is chosen to be 500 eV. Calculations are performed on all three *T*, *O*, and *R* phases of BTO. To simulate experimental doping concentrations, we adopt a supercell approach with periodic boundary conditions and perform our calculations using $2 \times 2 \times 3$, $3 \times 2 \times 1$, and $2 \times 2 \times 1$ supercells (Fig. S1 in the Supplemental Material [32]) corresponding to ferroelectric *T* (*P4mm*), *O* (*Amm2*), and *R* (*R3m*) phases, respectively. In each of these supercells, two Ba ions are replaced by two Ca ions and a single Ti ion is replaced by a single Zr ion. For structural optimization, we choose a convergence criterion of 10^{-6} eV for the self-consistent field (SCF) electronic energy and $10^{-3}\ \mathrm{eV\,A^{-1}}$ for the Hellmann-Feynman forces on each atom. Three $(8 \times 8 \times 8)$, $(6 \times 8 \times 8)$, and $(8 \times 8 \times 6)$ Monkhorst-Pack grids [33] are used for the Brillouin Zone integration of bulk *T*, *O*, and *R* BTO, respectively. Proportionate *k* grids are used for the super cells. The effective mass of electrons (m_e^*) and holes (m_h^*) at the band extrema, that is, around the conduction band minimum (CBM) or the valence band maximum (VBM) are calculated using the finite difference method as implemented in the effective mass calculator by Fonari and Sutton [34].

III. RESULT AND DISCUSSION

A. Structural, dielectric, ferroelectric, and optical studies

The XRD pattern recorded on the BZT-BCT sample at room temperature (approximately 27 °C) is shown in

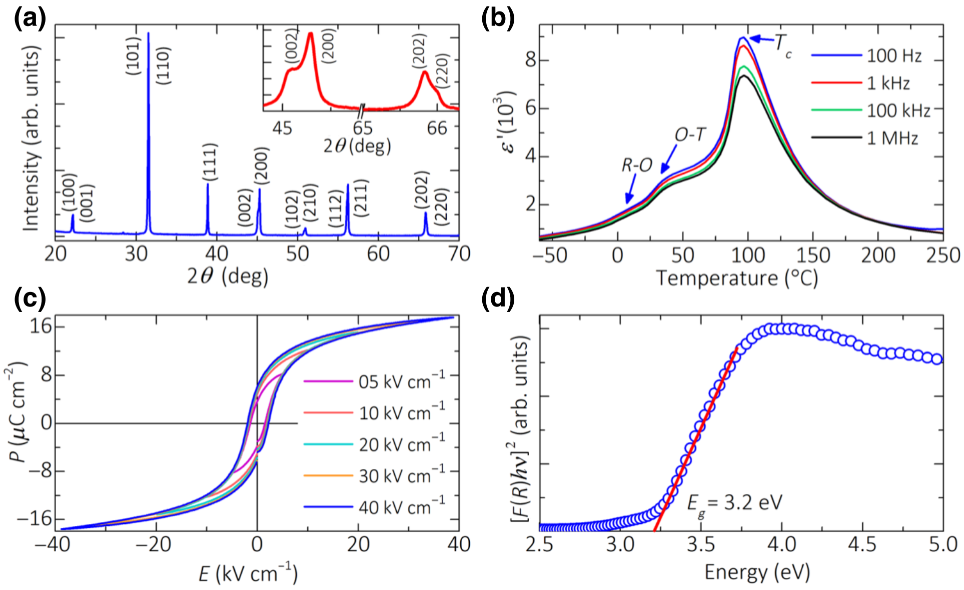

FIG. 1. (a) The XRD pattern of the BZT-BCT indexed to the tetragonal symmetry and (b) the temperature variation of a dielectric constant at different frequencies. The different phase transitions (*R* to *O*, *O* to *T* and *T* to cubic) are pointed out with arrow marks. (c) The polarization switching with respect to different electric fields at 10 Hz and (d) the optical band gap measured using Kubelka-Munk plot for the BZT-BCT ceramic.

Fig. 1(a) and confirms the phase formation of the compound without any secondary phases. Note that the BZT-BCT composition is at its MPB where the *R*, *O*, and *T* phases coexist. To confirm the coexisting phases, the XRD patterns of the {200} and {220} peaks are shown in the inset in Fig. 1(a). The merging of the tetragonal (002)/(200)

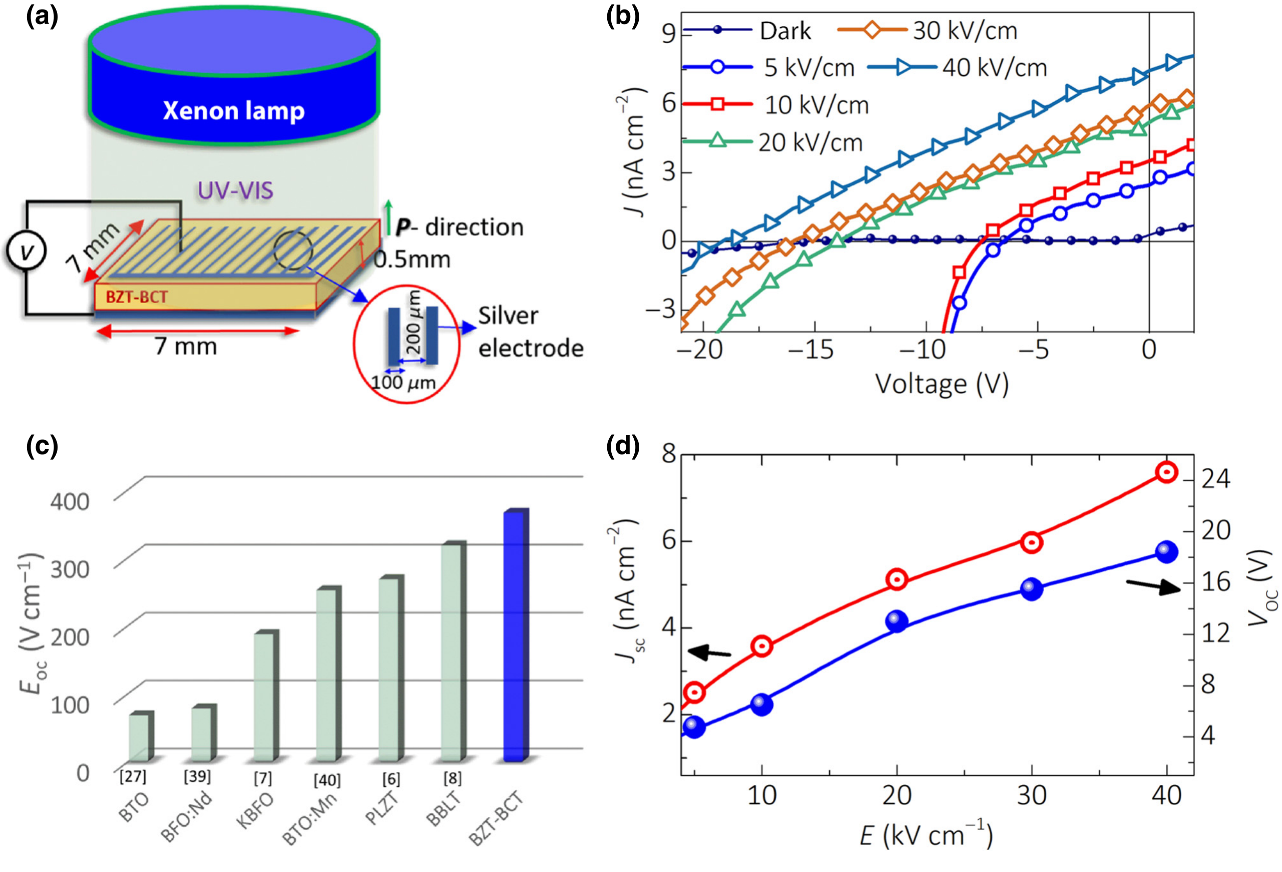

FIG. 2. (a) The schematic diagram for the photovoltaic measurement setup along with the sample geometry, (b) poling voltage variation of *I*-*V* characteristics under dark and light illumination, (c) the bar diagram of E_{OC} reported for different ferroelectric systems along with the present BZT-BCT sample, and (d) J_{SC} and V_{OC} vs poling electric field for BZT-BCT sample.

peaks and the asymmetric character of the (200) peak gives evidence for the existence of the *R* and *T* phases [35]. Correspondingly, the merging of (202)/(220) gives evidence for the presence of the *O* phase in BZT-BCT [36].

The dielectric constant measured in the temperature range of −60 °C to 250 °C at various frequencies (100 Hz to 1 MHz) are plotted in Fig. 1(b) and the plots reveal the signature of *R*-*O* and *O*-*T* phase transitions (marked by arrows) along with the ferroelectric Curie temperature (T_C) at 95 °C. The two broad *R*-*O* and *O*-*T* transitions located close to each other near room temperature give an additional indication for the coexisting phases [37]. The frequency independent nature of T_C and the subsequent dielectric dispersion shown in Fig. 1(b) reflect that the sample is an ergodic relaxor-type ferroelectric [24]. To characterize the ferroelectric properties, the polarization is plotted against the electric fields in Fig. 1(c). The evolution of the *P*-*E* loops with field and its well-saturated hysteresis character at high field confirm the ferroelectric characteristics of the sample. The sample shows maximum polarization (P_m) of 17.5 μC cm^{-2} at 40 kV cm^{-1}. To obtain the optical band gap, the reflectance spectrum recorded on the sample is converted into the Kubelka-Munk coefficient $[F(R)\ h\nu]^2$ and is plotted as a function of $h\nu$ in Fig. 1(d). The deduced band-gap value from the Kubelka-Munk plot is 3.2 eV [38].

B. Photovoltaic and structural studies

To carry out the photovoltaic measurements [shown as schematics in Fig. 2(a)], the BZT-BCT sample with Ag electrodes in finger geometry is poled at 40 kV cm^{-1} (well above its coercive field). The photograph of the sample with finger electrode geometry and the experimental set up used in the measurement can be seen (Fig. S2) in the Supplemental Material [32]. The current density (J_{SC}) vs bias voltage (V) measured under dark and light illumination conditions are shown in Fig. 2(b). The *J*-*V* curves reveal a large PV response with $V_{OC} = 18.4$ V ($E_{OC} = 368$ V cm^{-1}) and short-circuit current (J_{SC}) = 7 nA cm^{-2}.

The observed E_{OC} is one of the largest values reported among ferroelectric polycrystalline samples and is, in fact, a 400% increase in comparison to the value reported for a BTO single crystal of similar thickness [3]. The E_{OC} reported for several compounds are plotted as a bar diagram in Fig. 2(c), which highlights the importance of BZT-BCT polycrystalline sample as one of the potential

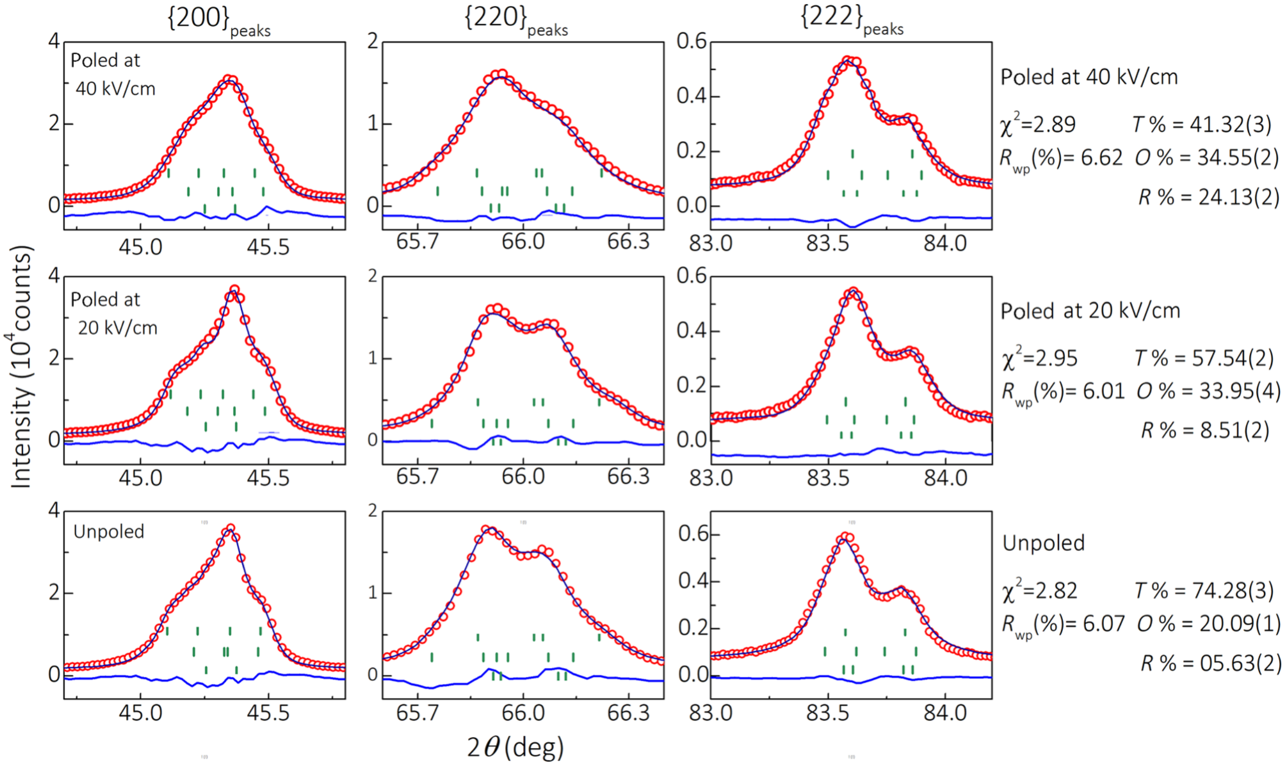

FIG. 3. Rietveld-refined XRD profiles for the family of significant peaks, {200}, {220}, and {222}, are presented for samples poled at 0, 20, and 40 kV cm^{-1}. The fitting is done by considering *T* (*P4mm*), *O* (*Amm2*), and *R* (*R3m*) phases. The corresponding refined parameters (χ^2, R_{wp}, and % phase fractions) are displayed on the right side of the figure. The red circles, black lines, and blue lines represent the measured and fitted data and their difference to XRD data, respectively. The green line symbols represent the peak positions.

PV materials among the existing perovskite ferroelectric systems [6–8,27,39,40].

A similar anomalous PV response observed in BTO [27], LNO [2], BBLT [8], and KBNNO [16] is attributed to the consequence of the shift-current phenomenon. In the shift-current mechanism, the driving force for carrier separation is coherent evolution of the electron and hole wave functions, which leads to the rapid propagation of carriers to the electrodes by minimizing the opportunity for energy losses and thereby giving a high V_{OC} [12]. Interestingly, the dependence of BPVE on the crystal structure, more precisely on the electronic structure, within the framework of shift-current theory has been elucidated by Wang and Rappe [18]. Their shift-current response and the calculated Glass coefficient in KNO at its different crystallographic phases revealed the dominance of the PV response in the *R* and *O* phases as compared to the *T* phase. Note that the evolution of structural phases under electric field-poling conditions in the morphotropic sample is well reported by many others [24–26]. In particular, the BZT-BCT sample is reported to show the transformation of a substantial fraction of the *T* phase into the *R* and *O* phases upon poling [24]. In fact, such a field-induced phase transformation is responsible for the large piezoelectric coefficient observed in BZT-BCT ceramic. Earlier reports on a large PV response in lanthanum-modified PZT near the MPB composition suggests that the difference in coexisting structural phases could play a major role in their PV response [19]. Additionally, the Schottky barrier formed at the metal/ferroelectric interface in a thin film could also play a significant role in the PV response. This effect is well established in Pt/BFO/$\mathrm{SrRuO_3}$ thin-film capacitor structures where polarization-modulated carrier injection at the interface is responsible for the photoresponse mimicking the polarization hysteresis loop behavior [41]. Similarly, the ferroelectric hysteretic PV behavior in $\mathrm{Bi_2FeCrO_6}$, which has recently been reported, can be used to develop the ferroelectric based solar cells [42]. However, the observed large PV response in a BZT-BCT sample over the BTO sample, despite both showing similar ferroelectric characteristics, indicates that the polarization and carrier injection at the interface layer alone is not responsible for such a large above band-gap PV response. In this context, to understand the effect of structural transformation due to poling on the PV effect, it would be interesting to carry out poling-dependent PV studies.

Hence, the PV measurements are performed on BZT-BCT samples poled at 5, 10, 20, 30, and 40 kV cm^{-1}, respectively. The resultant *J*-*V* plots are shown in Fig. 2(b). The obtained V_{OC} and J_{SC} plotted as a function of the poling field in Fig. 2(d) exhibit dramatic enhancement in the PV response where the V_{OC} changes from 7 to 18.4 V for the change in poling fields from 5 to 40 kV cm^{-1}, respectively. The plots of V_{OC} measured as a function of time under a light illumination condition shows a well-saturated value as shown in Fig. S3 of the Supplemental Material [32].

To quantify the transformed phases upon poling, XRD patterns are recorded on BZT-BCT samples subjected to 0, 10, 20, 30, and 40 kV cm^{-1} fields and the resultant plots are provided in Fig. S4 of the Supplemental Material [32]. Prior to the XRD measurements, the poled pellets are made into powder form to avoid the preferred orientation effect [24,26]. The patterns are refined using FULLPROF software and the best fit is achieved by considering the *T*, *O,* and *R* phases together. The complete refined parameters are given in Tables S1–S5 of the Supplemental Material for samples poled at 0, 10, 20, 30, and 40 kV cm^{-1} fields, respectively [32].

To realize the phase evolution, the refined XRD profile patterns for the three significant pseudocubic peaks, such as $\{200\}_{\mathrm{pc}}$, $\{220\}_{\mathrm{pc}}$, and $\{222\}_{\mathrm{pc}}$ of samples poled at 0, 20, and 40 kV cm^{-1} fields are shown in Fig. 3 along with the goodness of fit (χ^2), weighted profile *R* factor (R_{wp}), and % of phase fraction extracted from the refinement. [Note that the Rietveld refinement is carried out by including both $K_{\alpha 1}$ and $K_{\alpha 2}$ wavelengths]. The refinement confirms that the *T* phase with approximately 74% phase fraction is dominating over the *O* (approximately 20%) and *R*

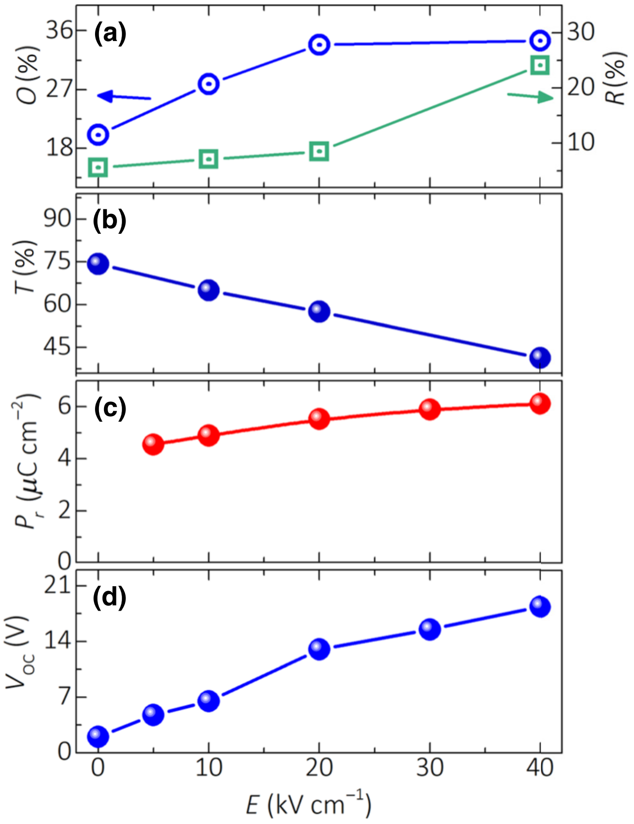

FIG. 4. The evolution of (a) the % of *O* and *R* phase fractions, (b) the % of *T* phase fraction, (c) P_r, and (d) V_{OC} as a function of poling field.

(approximately 6%) phases at the unpoled state. However, these phases undergo transformation due to poling. As a result, the *O* and *R* phases' fractions increase with poling at the expense of the *T* phase and the resultant evolutions of the phase fractions are shown in Figs. 4(a) and 4(b). The remnant polarization (P_r) and V_{OC} are also plotted as a function of the poling field in Figs. 4(c) and 4(d). Notably, the figure reveals that the variation of V_{OC} with poling field exhibits a remarkable similarity with *O* and *R* phase evolutions and this confirms the structural correlation with the photoresponse. On the other hand, the observed substantial increment in V_{OC} (5–18.4 V) while changing the poling field from 5 to 40 kV cm^{-1} could not be directly corroborated with the nominal change in remnant polarization P_r (4.5–5.9 μC cm^{-2}) displayed at the same field range [see Fig. 4(c)]. These findings demonstrate that although polarization may play a role in PV response at a low electric field, the major contribution is attributed to the preferable structural symmetry and the associated electronic properties. This can be established well by band-structure calculations for different coexisting phases via DFT.

C. DFT band structure and effective mass analysis

To probe how the symmetry breaking affects the electronic structure and, in turn, changes the PV response, we have carried out DFT calculations (details are given in the computational section) on the *T*, *O*, and *R* phases of the BZT-BCT compound. Figure 5 shows the band structure as well as the projected density of states (PDOS) and charge density contours to highlight the orbital composition in the vicinity of the CBM. The band structure reveals that the lower lying conduction band and upper lying valence bands are comparatively more dispersive in the *T* phase. However, due to the symmetry reason, these bands are

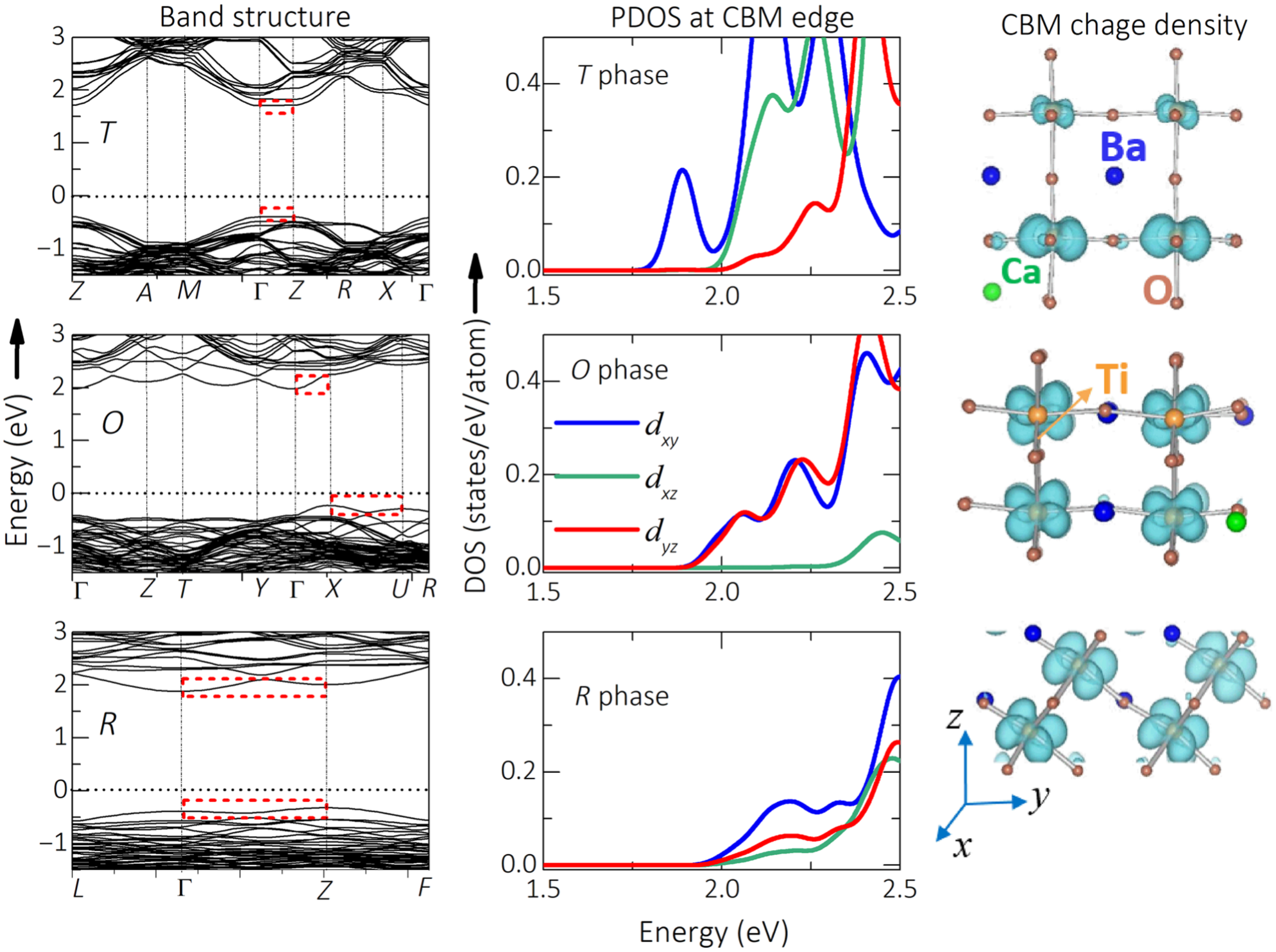

FIG. 5. (left panel) The band structure for the different phases of BZT-BCT with space group of *P4mm* (*T*), *Amm2* (*O*), and *R3m* (*R*). (middle panel) Ti-*d* partial densities of states and (right panel) the charge density in the vicinity of CBM for the *T*, *O*, and *R* phases. The mixing of the d_{xy} and $d_{xz/yz}$ orbitals in the *R* and *O* phases is evident compared to the well-separated d_{xy} and $d_{xz/yz}$ states in the *T* phase. These are reflected in the CBM charge density of the corresponding phases. The delocalization and reorientation of charge density in *R* and *O* phases favors a high PV response.

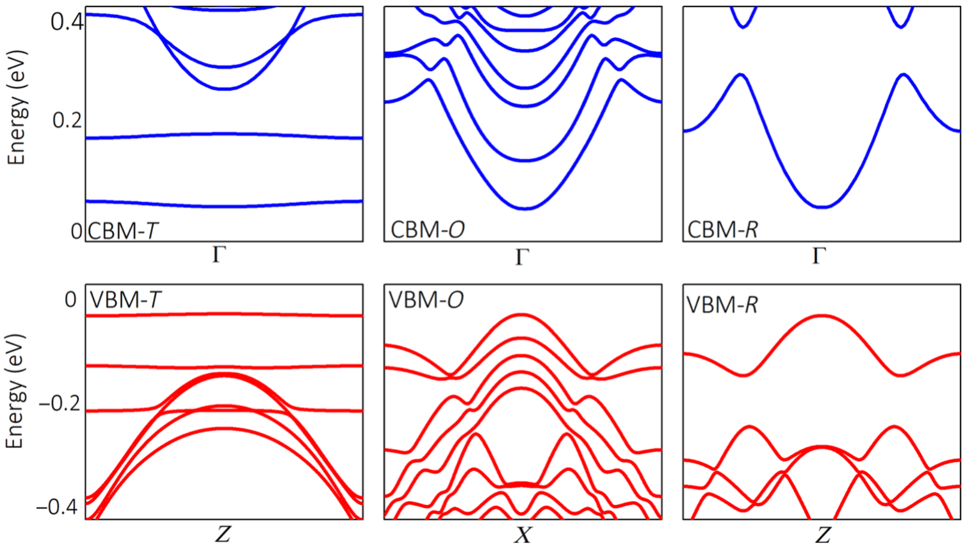

FIG. 6. The band dispersion of the T, O, and R phases of BZT-BCT around band extrema and along the z direction. The weakly dispersed band for both CBM and VBM of the T phase will lead to larger electron and hole effective masses, respectively, thus lowering the mobility of the photoexcited charge carriers along the z direction. However, both CBM and VBM of the R and O phases are highly dispersive, indicating a reduction in the hole and electron effective masses. This substantially increases the mobility of charge carrier along the z direction.

nondispersive along the z direction (i.e., along Γ–Z) for the T phase. From the projected DOS and charge densities, we find that, in this case, the CBM are occupied by the antibonding Ti$-d_{xy}$ states while the $d_{xz/yz}$ orbitals occupy at a higher energy, resulting in the splitting of the d_{xy} and $d_{xz/yz}$ orbitals.

However, in both the O and R phases, due to a change in the crystal field, there is a larger hybridization among the d_{xy}, and $d_{xz/yz}$ orbitals, leading to a mixing of these orbital characters in the CBM. Such a mixing of orbitals is also clearly evident in corresponding CBM charge densities. The band dispersions along the Γ–Z confirms the hybridization of these orbitals. According to shift current theory, if the CBM is more occupied by z axis-oriented orbitals (e.g., d_{xz}, d_{yz}, d_{z2-1}) and is very much delocalized due to stronger covalent interaction along the polarization direction (along the z axis), then the shift current response is high and a large BPVE is observed [8,13,14,18,43]. Therefore, the PV response is enhanced in both the O and R phases compared to that of the T phase. These results are in good agreement with our experimental observations.

Additionally, the important dynamical factor, which will affect the PV response of the material, is the mobility of the photogenerated charge carriers. In general, a higher mobility denotes suppression of charge-carrier recombination and hence enhances the PV response [44]. The effective mass is defined as $1/m^* = 1/h^2(\partial^2 E_n(k)/\partial^2 k_i k_j)$ where $i,j = x,y,z$ of the charge carriers and is inversely proportional to its mobility. Materials with a lighter effective mass and hence higher mobility are preferred for better PV response [44]. The effective masses are highly anisotropic due to direction-dependent band dispersion in k space.

TABLE I. The m_e^* and m_h^* of BZT-BCT for different phases.

Phase	Effective mass (m_o)	x	y	z
T	m_e^*	0.165	0.590	3.258
	m_h^*	−0.271	−0.979	−8.703
R	m_e^*	0.338	0.200	0.221
	m_h^*	−0.463	−0.294	−0.394
O	m_e^*	0.166	0.321	0.285
	m_h^*	−0.253	−0.467	−0.480

In a ferroelectric material such as BTO, the effective mass along the z direction (along the direction of current flow) is important for better PV response. Figure 6 shows the band dispersion of T, O, and R phases centering on CBM and VBM along the z direction in the reciprocal space. The flat CBM dispersion for the T phase compared to highly dispersive bands for the O and R phases suggests low electron effective masses for both R and O phases. The calculated effective mass values for all three phases are given in Table I. Note that the calculations done on bulk BTO show that the effective mass for the T phase is in agreement with already reported theoretical and experimental results [33]. In the T phase of BZT-BCT, since electron charge density is delocalized along the x and y directions (Fig. 5), the effective mass is 3.25 m_o (where m_o is the mass of electron) for electrons in the z direction, which is much larger compared to that in the x and y directions (see Table I). However, for O and R phases, the effective mass along the z direction is around one order lower than that of the corresponding T phases (see Table I). From Table I and Fig. S5 within the Supplemental Material [32], we observe a similar trend for the hole effective mass as well. Hence, both R and O phases should show better PV responses compared to that of the T phase.

D. Photocurrent response

The BPVE of the BZT-BCT sample shows a unique current behavior upon light in the *on* and *off* states. The J_{SC}

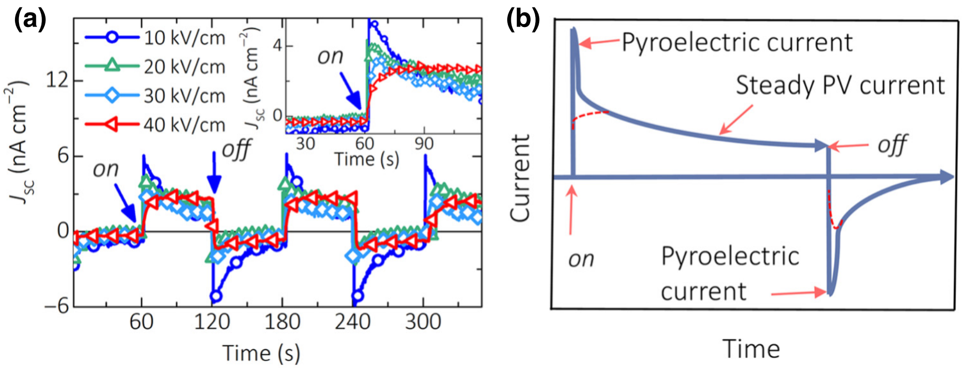

FIG. 7. (a) The sharp photo current responses of BZT-BCT compound at different poling fields and (b) the schematically shown pyroelectric and steady-state photocurrent nature, with light in the *on* and *off* states in photovoltaic measurement.

vs time plot, shown in Fig. 7(a) for samples poled at different fields, reveals a jump in current when the light is *on* followed by a decreasing trend until reaching a steady state. A similar but reversed trend is observed when the light is in the *off* state and the current decays to zero after some time. Note that the generated current is a coupled phenomenon involving pyroelectric and photovoltaic currents [45], where the former is responsible for the initial current's shoot up and down during *on* and *off* states and the latter for the steady-state current as shown in the schematic in Fig. 7(b). The existence of a space charge and the related pyroelectric current contribution to the photocurrent in a BTO crystal, even above Curie temperature, is established by Chynoweth [45]. The pyrocurrent contribution decreases with an increase in the poling field and vanishes at the highest poling field [the inset of Fig. 7(a)]. Overall, the current *on* and *off* measurements on the BZT-BCT sample poled under different fields elucidate the roles of space charge and polarization field.

IV. CONCLUSION

In summary, we discover a large photogenerated electric field (368 V cm^{-1}) in BZT-BCT ferroelectric ceramic. The XRD analysis on the samples reveals the structural transformation of the T phase into O and R phases upon electric poling. In addition to this structural transformation, the increase in poling field demonstrates a systematic increase in V_{OC}, which implies the strong correlation between the structural phase transformation and PV response. These experimental results establish the fact that R and O symmetries are favorable for enhanced PV characteristics in BZT-BCT samples. The DFT calculations on this system predict that although CBM is composed of Ti t_{2g} (d_{xy}, d_{yz}, and d_{xz}) states, in general, the variation in the individual orbital contributions in forming the CBM makes the difference. Specifically, for the O and R phases, the d_{yz} and d_{xz} orbitals contributions are substantial enough to generate a large BPVE. Furthermore, the reduced effective mass along the direction of polarization for the O and R phases suggests that the states around the Fermi energy are more delocalized and hence, reduce the charge recombination rate, which is responsible for the achieved high PV response. Overall, the established giant photovoltaic response in the BZT-BCT system and its structural correlation point toward an alternative direction to achieve a high PV response and enable its applications in devices such as an UV detector, a photo-driven micro-sensor, a microactuator, and so on.

ACKNOWLEDGMENTS

We acknowledge Professor M.S.R. Rao and Dr. Martando Rath for the *P-E* measurements. Dr. D. Murali acknowledges CSIR, New Delhi, for financial support through SRA (Scientist Pool Scheme).

[1] P. Lopez-Varo, L. Bertoluzzi, J. Bisquert, M. Alexe, M. Coll, J. Huang, J. A. Jimenez-Tejada, T. Kirchartz, R. Nechache, F. Rosei, and Y. Yuan, Physical aspects of ferroelectric semiconductors for photovoltaic solar energy conversion, Phys. Rep. **653**, 1 (2016).

[2] V. M. Fridkin and B. N. Popov, Anomalous photovoltaic effect in ferroelectrics, Phys. Status Solidi A **46**, 729 (1978).

[3] J. E. Spanier, V. M. Fridkin, A. M. Rappe, A. R. Akbashev, A. Polemi, Y. Qi, Z. Gu, S. M. Young, C. J. Hawley, D. Imbrenda, G. Xiao, A. L. Bennett-Jackson, and C. L. Johnson, Power conversion efficiency exceeding the Shockley-Queisser limit in a ferroelectric insulator, Nat. Photonics **10**, 611 (2016).

[4] H. T. Yi, T. Choi, S. G. Choi, Y. S. Oh, and S. W. Cheong, Mechanism of the switchable photovoltaic effect in ferroelectric BiFeO$_3$, Adv. Mater. **23**, 3403 (2011).

[5] X. Yang, X. Su, M. Shen, F. Zheng, Y. Xin, L. Zhang, M. Hua, Y. Chen, and V. G. Harris, Enhancement of photocurrent in ferroelectric films via the incorporation of narrow bandgap nanoparticles, Adv. Mater. **24**, 1202 (2012).

[6] J. Zhang, X. Su, M. Shen, Z. Dai, L. Zhang, X. He, W. Cheng, M. Cao, and G. Zou, Enlarging photovoltaic effect: Combination of classic photoelectric and ferroelectric photovoltaic effects, Sci. Rep. **3**, 2109 (2013).

[7] G. Zhang, H. Wu, G. Li, Q. Huang, C. Yang, F. Huang, F. Liao, and J. Lin, New high T_{C} multiferroics KBiFe$_2$O$_5$

with narrow band gap and promising photovoltaic effect, Sci. Rep. **3**, 1265 (2013).

[8] S. Pal, A. B. Swain, P. P. Biswas, D. Murali, A. Pal, B. R. K. Nanda, and P. Murugavel, Giant photovoltaic response in band engineered ferroelectric perovskite, Sci. Rep. **8**, 8005 (2018).

[9] Y. Yuan, Z. Xiao, B. Yang, and J. Huang, Arising applications of ferroelectric materials in photovoltaic devices, J. Mater. Chem. A **2**, 6027 (2014).

[10] C. Paillard, X. Bai, I. C. Infante, M. Guennou, G. Geneste, M. Alexe, J. Kreisel, and B. Dkhil, Photovoltaics with ferroelectrics: Current status and beyond, Adv. Mater. **28**, 5153 (2016).

[11] P. S. Brody and F. Crowne, Mechanism for the high voltage photovoltaic effect in ceramic ferroelectrics, J. Electr. Mater. **4**, 955 (1975).

[12] K. Uchino, Y. Miyazawa, and S. Nomura, High-voltage photovoltaic effect in $PbTiO_3$-based ceramics, Jpn. J. Appl. Phys. **21**, 1671 (1982).

[13] L. Z. Tan, F. Zheng, S. M. Young, F. Wang, S. Liu, and A. M. Rappe, Shift current bulk photovoltaic effect in polar materials—hybrid and oxide perovskites and beyond, NPJ Comput. Mater. **2**, 16026 (2016).

[14] S. M. Young and A. M. Rappe, First Principles Calculation of the Shift Current Photovoltaic Effect in Ferroelectrics, Phys. Rev. Lett. **109**, 116601 (2012).

[15] M. Nakamura, S. Horiuchi, F. Kagawa, N. Ogawa, T. Kurumaji, Y. Tokura, and M. Kawasaki, Shift current photovoltaic effect in a ferroelectric charge-transfer complex, Nat. Commun. **8**, 1 (2017).

[16] A. Zenkevich, Y. Matveyev, K. Maksimova, R. Gaynutdinov, A. Tolstikhina, and V. Fridkin, Giant bulk photovoltaic effect in thin ferroelectric $BaTiO_3$ films, Phys. Rev. B **90**, 161409 (2014).

[17] A. M. Glass, D. Von Der Linde, and T. J. Negran, High-voltage bulk photovoltaic effect and the photorefractive process in $LiNbO_3$, Appl. Phys. Lett. **25**, 233 (1974).

[18] F. Wang and A. M. Rappe, First-principles calculation of the bulk photovoltaic effect in $KNbO_3$ and $(K,Ba)(Ni,Nb)O_{3-\delta}$, Phys. Rev. B **91**, 165124 (2015).

[19] P. Poosanaas and K. Uchino, Photostrictive effect in lanthanum-modified lead zirconate titanate ceramics near the morphotropic phase boundary, Mater. Chem. Phys. **61**, 36 (1999).

[20] W. Liu and X. Ren, Large Piezoelectric Effect in Pb-Free Ceramics, Phys. Rev. Lett. **103**, 257602 (2009).

[21] Z. Sun, C. Ma, M. Liu, J. Cui, L. Lu, J. Lu, X. Lou, L. Jin, H. Wang, and C. L. Jia, Ultrahigh energy storage performance of lead-free oxide multilayer film capacitors via interface engineering, Adv. Mater. **29**, 4 (2017).

[22] B. Asbani, J. L. Dellis, A. Lahmar, M. Courty, M. Amjoud, Y. Gagou, K. Djellab, D. Mezzane, Z. Kutnjak, and M. El Marssi, Lead-free $Ba_{0.8}Ca_{0.2}(Zr_xTi_{1-x})O_3$ ceramics with large electrocaloric effect, Appl. Phys. Lett. **106**, 042902 (2015).

[23] A. D. Dupuy, Y. Kodera, and J. E. Garay, Unprecedented electro-optic performance in lead-free transparent ceramics, Adv. Mater. **28**, 7970 (2016).

[24] K. Brajesh, K. Tanwar, M. Abebe, and R. Ranjan, Relaxor ferroelectricity and electric-field-driven structural transformation in the giant lead-free piezoelectric (Ba,Ca)$(Ti,Zr)O_3$, Phys. Rev. B **92**, 224112 (2015).

[25] L. Bellaiche, A. García, and D. Vanderbilt, Electric-field induced polarization paths in $Pb(Zr_{1-x}Ti_x)O_3$ alloys, Phys. Rev. B **64**, 060103 (2001).

[26] B. N. Rao and R. Ranjan, Electric-field-driven monoclinic-to-rhombohedral transformation in $(Na_{1/2}Bi_{3/2})TiO_3$, Phys. Rev. B **86**, 134103 (2012).

[27] W. T. H. Koch, R. Munser, W. Ruppel, and P. Würfel, Bulk photovoltaic effect in $BaTiO_3$, Solid State Commun. **17**, 847 (1975).

[28] G. Kresse and J. Furthmüller, Efficient iterative schemes for *ab initio* total-energy calculations using a plane-wave basis set, Phys. Rev. B **54**, 11169 (1996).

[29] G. Kresse and D. Joubert, From ultrasoft pseudo-potentials to the projector augmented-wave method, Phys. Rev. B **59**, 1758 (1999).

[30] J. P. Perdew, K. Burke, and M. Ernzerhof, Generalized Gradient Approximation made Simple, Phys. Rev. Lett. **77**, 3865 (1996).

[31] H. J. Monkhorst and J. D. Pack, Special points for Brillouin-zone integrations, Phys. Rev. B **16**, 1748 (1977).

[32] See Supplemental Material at http://link.aps.org/supplemental/10.1103/PhysRevApplied.11.044007 for the detailed data related to supercells used for the DFT calculations for different phases, photovoltaic experimental setup, sample geometry, XRD refinements, valance band PDOS and the tables containing refinement parameters for the presented sample.

[33] D. Bagayoko, G. L. Zhao, J. D. Fan, and J. T. Wang, *ab-initio* calculations of the electronic structure and optical properties of ferroelectric tetragonal $BaTiO_3$, J. Phys.: Condens. Matter **10**, 5645 (1998).

[34] A. Fonari and C. Sutton, Effective Mass Calculator (2012).

[35] K. H. Yoon and H. R. Lee, Electric-field-induced strain and piezoelectric properties near the morphotropic phase boundary of $Pb(Mg_{1/3}Nb_{2/3})O_3$–$PbZrO_3$–$PbTiO_3$ ceramics, J. Appl. Phys. **89**, 3915 (2001).

[36] W. Li, Z. Xu, R. Chy, P. Fu, and G. Zang, Polymorphic phase transition and piezoeletric propertes of $(Ba_{1-x}Ca_x)(Ti_{0.9}Zr_{0.1})O_3$ lead free ceramic, Physica B **405**, 4513 (2010).

[37] L. Zhang, M. Zhang, L. Wang, C. Zhou, Z. Zhang, Y. Yao, L. Zhang, D. Xue, X. Lou, and X. Ren, Phase transitions and the piezoelectricity around morphotropic phase boundary in $Ba(Zr_{0.2}Ti_{0.8})O_3$-$x(Ba_{0.7}Ca_{0.3})TiO_3$ lead-free solid solution, Appl. Phys. Lett. **105**, 2012 (2014).

[38] H. S. Kim, C. R. Lee, J. H. Im, K. B. Lee, T. Moehl, A. Marchioro, S. J. Moon, R. Humphry-Baker, J. H. Yum, J. E. Moser, M. Grätzel, and N. G. Park, Lead iodide perovskite sensitized all-solid-state submicron thin film mesoscopic solar cell with efficiency exceeding 9%, Sci. Rep. **2**, 291 (2012).

[39] Y.-T. Peng, S.-H. Chiou, C.-H. Hsiao, C. (Hao) Ouyang, and C.-S. Tu, Remarkably enhanced photovoltaic effects and first-principles calculations in neodymium doped $BiFeO_3$, Sci. Rep. **7**, 45164 (2017).

[40] R. Inoue, S. Ishikawa, R. Imura, Y. Kitanaka, T. Oguchi, Y. Noguchi, and M. Miyayama, Giant photovoltaic effect of ferroelectric domain walls in perovskite single crystals, Sci. Rep. **5**, 14741 (2015).

[41] D. Lee, S. H. Back, T. H. Kim, J.-G. Yoon, C. M. Folkman, C. B. Eom, and T. W. Noh, Polarity control of carrier injection at ferroelectric/metal interfaces for electrically switchable diode and photovoltaic effects, Phys. Rev. B **84**, 125305 (2011).

[42] A. Quattropani, A. S. Markhort, M. V. Rastei, G. Versini, G. Schmerber, S. Barre, A. Dinia, A. Slaoui, J. L. Rehspringer, T. F. Colis, and B. Kundys, Tuning photovoltaic response in Bi_2FeCrO_6 films by ferroelectric poling, Nanoscale **10**, 13761 (2018).

[43] S. M. Young, F. Zheng, and A. M. Rappe, First-Principles Calculation of the Bulk Photovoltaic Effect in Bismuth Ferrite, Phys. Rev. Lett. **109**, 236601 (2012).

[44] J. Zhang, P. Zhou, J. Liu, and J. Yu, New understanding of the difference of photocatalytic activity among anatase, rutile and brookite TiO_2, Phys. Chem. Chem. Phys. **16**, 20382 (2014).

[45] A. G. Chynoweth, Surface Space-Charge Layers in Barium titanate, Phys. Rev. B **102**, 3 (1955).